CrossMark

Observation and numerical modeling of tidal dune dynamics

Arnaud Doré[1] · Philippe Bonneton[2] · Vincent Marieu[2] · Thierry Garlan[3]

Abstract

Tidal sand dune dynamics is observed for two tidal cycles in the Arcachon tidal inlet, southwest France. An array of instruments is deployed to measure bathymetric and current variations along dune profiles. Based on the measurements, dune crest horizontal and vertical displacements are quantified and show important dynamics in phase with tidal currents. We observed superimposed ripples on the dune stoss side and front, migrating and changing polarity as tidal currents reverse. A 2D RANS numerical model is used to simulate the morphodynamic evolution of a flat non-cohesive sand bed submitted to a tidal current. The model reproduces the bed evolution until a field of sand bedforms is obtained that are comparable with observed superimposed ripples in terms of geometrical dimensions and dynamics. The model is then applied to simulate the dynamics of a field of large sand dunes of similar size as the dunes observed in situ. In both cases, simulation results compare well with measurements qualitatively and quantitatively. This research allows for a better understanding of tidal sand dune and superimposed ripple morphodynamics and opens new perspectives for the use of numerical models to predict their evolution.

Keywords Dunes · Ripples · Sediment transport · Morphodynamics · Measurements · Tide · Numerical modeling

1 Introduction

Sand dunes are ubiquitous in natural subaqueous environments (Best 2005) and are commonly observed in coastal areas (Langhorne 1982; Ernstsen et al. 2006; Li et al. 2014). Sand dunes may pose a significant risk in coastal

✉ Arnaud Doré
ard@dhigroup.com

✉ Philippe Bonneton
philippe.bonneton@u–bordeaux.fr

Vincent Marieu
vincent.marieu@u-bordeaux.fr

Thierry Garlan
garlan@shom.fr

[1] Danish Hydraulics Institute, Agern Allé 5, 2970 Hørsholm, Denmark

[2] Université de Bordeaux, CNRS; UMR 5805-EPOC, 33405 Talence, France

[3] SHOM; HOM/REC-CFuD/Sédimentologie, CS 92803, 29228 Brest Cedex 2, France

environments for many domains such as the offshore industry (Whitehouse et al. 2000; Morelissen et al. 2003), navigation (Knappen and Hulscher 2002; Vantorre et al. 2013), or marine renewable energies (Barrie et al. 2005; Todd et al. 2014; Barrie and Conway 2014). Sand dunes in coastal areas present a high degree of heterogeneity, which is due to the spatiotemporal variability of forcing conditions, the type and quantity of sediment, and a history of evolution (Rubin and McCulloch 1980; Belderson et al. 1982; Li et al. 2014).

Observations show that in areas where dunes are present, currents are moderate enough to allow sediment deposition and high enough to allow bedform generation. Adimensional shear velocities generally remain under a threshold of $u^*/u_c^* \approx$ 3–4 (Barnard et al. 2006; Li et al. 2014), with u^* the shear velocity and u_c^* the critical shear velocity for sediment motion. If this threshold is exceeded, fine-to-medium sands are dispersed and dunes cannot develop (Doré 2015). The spatial distribution of tidal current intensity and direction and the type of sediment substrate determine the shape and the number of dunes (Belderson et al. 1982; Todd 2005). Dreano et al. (2010) showed for various experiments the role of the quantity of sediment and of the current intensity in controlling dune shapes, obtaining realistic bedforms when compared to bedforms in natural environments. Dune geometrical dimensions are

linked to the water depth, D (Charru 2013). Within tidal channels of depths of the order of tens of meters, dune wavelengths and heights are of the order of tens of meters and a few meters, respectively (Thauront 1995; Ernstsen et al. 2006). Dune size varies with sediment roughness and quantity and spatiotemporal variations of hydrodynamic forcing conditions, leading to local variations of one up to two orders of magnitude (Li et al. 2014). At the scale of a tidal cycle, the dune profile will adapt to quick variations of the current intensity and the water depth, between two slack tides. In tidal environments, at depths around 15 m, some authors measured horizontal dune crest displacements up to 3 m and vertical displacement of a few tens of centimeters (Langhorne 1982; Ernstsen et al. 2006). Observations showed that dune front slopes of ebb-oriented dunes are steeper during ebb tides, with values up to 15°–20°, and that a recirculation cell can develop intermittently downstream of crests (Kostaschuk and Best 2005; Ernstsen et al. 2006; Lefebvre et al. 2013). Superimposed ripples are migrating on dune profiles, with varying orientation and migration rates (Knaapen et al. 2002; Ernstsen et al. 2006; Barnard et al. 2012).

Observations of bedform development under various flow conditions show that an initially flat bed evolves through different phases: an incipient bedform phase, a growing bedform phase, and a stabilizing phase leading to a fully developed dune field (Baas 1994, 1999; Perillo et al. 2014). The presence of dune fields on the bottom leads to an increase of the flow resistance (Engelund 1966; Fredsøe and Deigaard 1992). Understanding dune evolution is therefore an important issue to accurately predict the flow circulation, sediment fluxes, and the bathymetric variations. The morphodynamic evolution of subaqueous sand dunes has been extensively studied during controlled experiments (Coleman and Melville 1996; Langlois and Valance 2007; Fourrière et al., 2010) or in numerical modeling studies mostly for steady current conditions (Niemann et al. 2011; Nabi et al. 2013; Doré et al. 2016). Doré et al. (2016), using a 2D RANS model, reproduced the different phases of evolution of an erodible sand bed until a dune field in equilibrium with the flow was obtained.

Sand dunes in tidal environments present a higher degree of complexity than those in flume experiments, which is due to the spatiotemporal variability of forcing conditions, the type and quantity of sediment, and a history of evolution (Rubin and McCulloch 1980; Belderson et al. 1982; Best 2005; Li et al. 2014). To date, no numerical model exists that can simulate tidal sand dune evolution.

In the next section, we present measurement results carried out in the southern pass of the Arcachon inlet and analyze sand dune and superimposed ripple dynamics for two tidal cycles. Then, in Section 3, we introduce a 2D RANS numerical model that is used to simulate sand ripple and dune morphodynamics submitted to tidal current conditions for several tides.

2 Observation of short-term tidal dune dynamics

2.1 Study area

The Arcachon lagoon is situated on the southwest coast of France and communicates with the Atlantic Ocean through a tidal inlet of an average width of 3 km (Fig. 1). The tidal range varies from 0.8 to 4.6 m for neap and spring tides, respectively. The mouth of the lagoon has a complex and active morphology, with a vast ensemble of sand banks, fed by an important southward littoral drift and shaped by highly energetic waves from the northwest with an annual significative height of $H_s = 1.36$ m and average peak period of $T_p = 6.5$ s (Butel et al. 2002). The tidal inlet is composed of a northern and a southern channel, with maximum depth averaged current velocities up to 2 and 1.4 m s^{-1}, respectively (Pedreros et al. 2008). The study area is located in the southern pass, between a sand bank (Arguin sand bank) and the southern shore of the inlet. Thauront (1995) conducted lateral sonar measurements and observed sand dunes on the bottom of both channels. The area is rich in non-cohesive sediment, with strong tidal currents, and is sheltered from the waves, insuring mostly unidirectional tidal forcing conditions. The bottom of the southern pass was also well preserved from human intervention (Doré 2015). The width of the southern pass near the study area varies between 750 and 850 m.

2.2 Material and methods

Seven measurement campaigns were carried out in the inlet of the Arcachon lagoon between April 2013 and June 2014 to study tidal dune dynamics. We used a bi-frequency *Odom Echotrack* echosounder from *Teledyne Marine* linked to a *Leica GS 15* GPS to measure the water depth along bathymetry transects in the study area at different dates. The vertical resolution of the measure is 0.1% of the water depth, according to the constructor, leading to a centimetric precision of measures in the southern pass of the Arcachon inlet. A preselected dune profile was measured during two tides of different intensities, for the mean tide of September 14, 2013, and the spring tide of June 13, 2014, to evaluate dune and superimposed ripple short-term dynamics. Current velocities along the dune profile were measured with a ship mounted ADCP *RDI Rio Grande*. An ultrasound altimeter ALTUS from *NKE* was deployed on the dune profile to detect the migration of superimposed bedforms. We placed a tripod structure mounted with an ADCP *Workhorse Sentinel* of *RD Instruments* and an ADV of *VECTOR-NORTEK*, close to the dune crest, to measure boundary layer currents for a full spring-neap tidal cycle, with a vertical resolution along the water column of 0.5 m. The full experimental design is shown in Fig. 2.
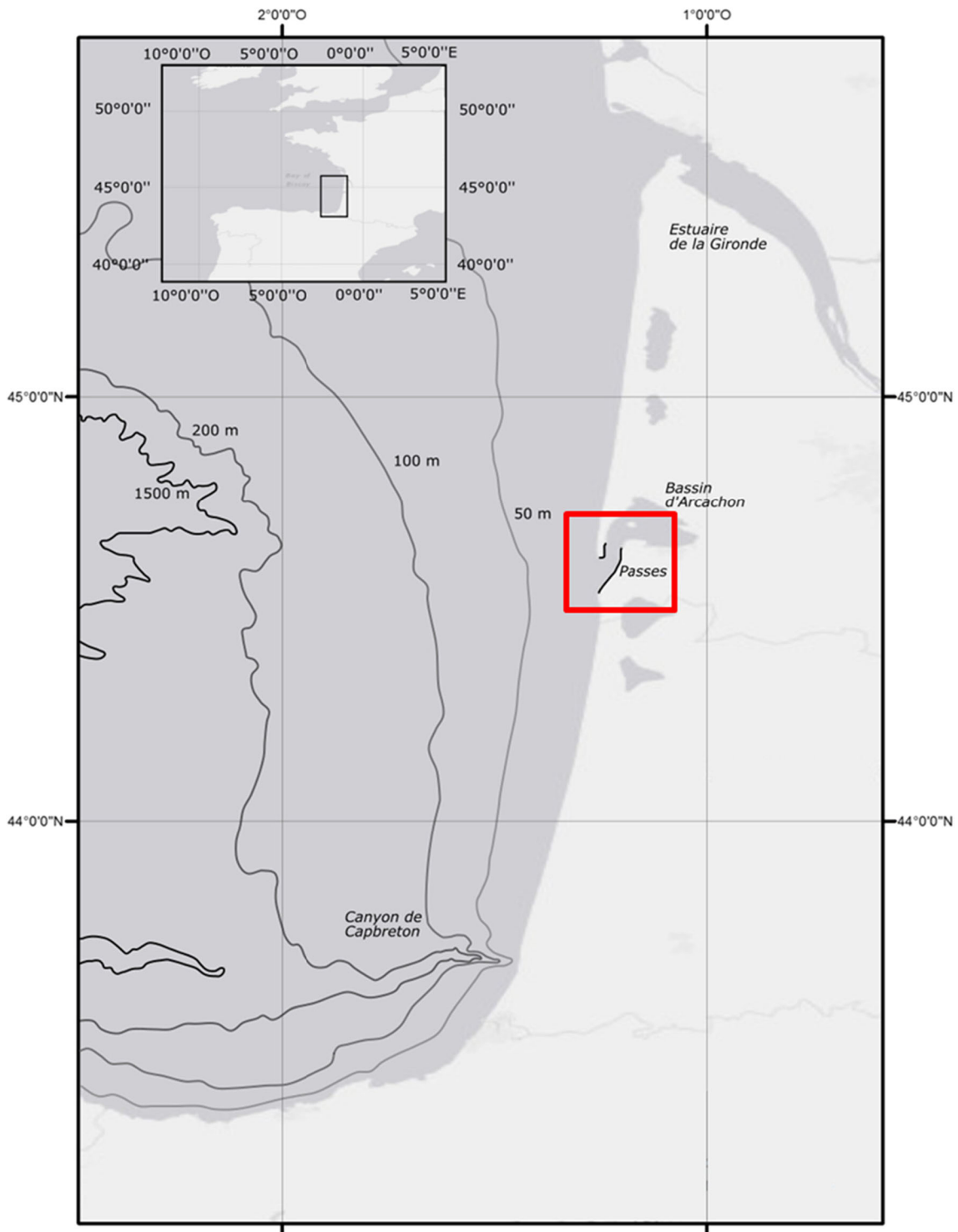
Fig. 1 Location of the study area in southwest France (red square)

2.3 Bathymetry

The bathymetry was first measured over a large area during three preliminary campaigns, between April 22, 2013, and July 08, 2013. The interpolated data showed a field of large bedforms with crests spaced by several tens of meters and covering the sandy bottom. Bedforms in the southern pass have asymmetrical profiles oriented towards the southwest, in the ebb flow direction. Crest heights of a couple of meters gradually decrease from the middle of the channel towards the edges, where the positions of the crests are also more advanced and more spaced. A Fourier spectral analysis of the bottom
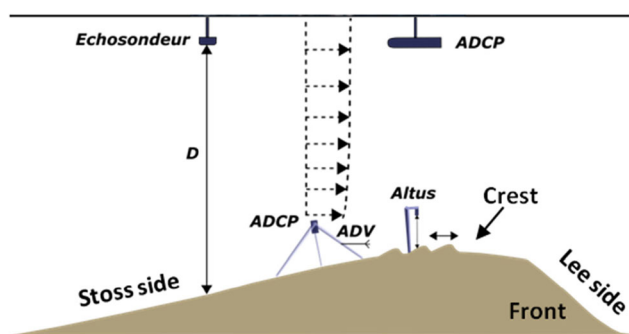
Fig. 2 Sketch of the experimental design with instruments deployed during measurement campaigns

revealed two main peaks of energy around $\lambda = 70$ m and $\lambda = 105$ m, λ being the wavelength in the middle and in the edges of the channel, respectively. Considering a mean water depth of $\overline{D} = 13$ m, these wavelengths correspond to the values of the adimensional depth $k\overline{D}$ around unity, k being the wave number, which is the signature of a dune mode (Fourrière et al. 2010). The lower and more spaced dune crests in the channel edges are characteristic of a milieu that is poorer in sediment (Dreano et al. 2010; Li et al. 2014). Lateral sonar measurements by Thauront (1995) showed the presence of coarser sediments on each side of the channel. The bathymetry was measured again on September 13, 2013, in a smaller area to select a dune profile and study its dynamics (Fig. 3).

2.4 Results

The dune profile was observed for a tide of moderate tidal range (mean tide) on September 24, 2013 (Fig. 4), and for a spring tide on June 13, 2014 (Fig. 5). ADCP measurements

above the crest show that horizontal current velocities lie in the interval 0.8 m s^{-1} < U_0 < 1.3 m s^{-1}, with U_0 the horizontal current velocities, for neap and spring tides, respectively. Currents are oriented in the direction of the channel axis, with main directions $\theta = 35°$ and $\theta = 215°$ during ebb and flood tides, respectively. Currents are oriented towards the flow 55% of the time, although currents of higher intensities occur during ebb tides, explaining that dunes have ebb-oriented crests. Values of Froude numbers above the crest are small, with $\overline{Fr} \approx 0.1$, leading to weak deformations of the free surface (Fredsøe 1982). Measurements along the dune profile with the embarked ADCP showed that horizontal velocities increase along the dune profile from 0.5–1 m s^{-1} to 1–1.5 m s^{-1}, in the vicinity of the trough and the crest, respectively.

Measurements carried out during the mean tide of September 24 covered the second half of the ebb tide (3 h before low tide) and 1.5 h after the beginning of the flow. Figure 4 shows the position of the crest, C, and of a superimposed ripple, R, located close to the trough. R is clearly changing polarity between the ebb and the flow phases. The weak migration rate of R could not be assessed. The dune profile keeps an asymmetry in the direction of the ebb tide, even during the flood tide. The dune front has a gentle slope of around 5°, which is weakly varying during the tidal cycle. The profile is bended on the stoss side, mostly during the flow, between $x = 70$ m and $x = 80$ m, x being the abscissa perpendicular to the dune front. This "cat-back"-shaped dune profile has already been described by Langhorne (1982) but is not well understood. The profile slope in the vicinity of the crest on the dune stoss side is higher than 15° during the flow, which is above the threshold value for the existence of a flow recirculation cell (Paarlberg et al. 2009). Such a recirculation
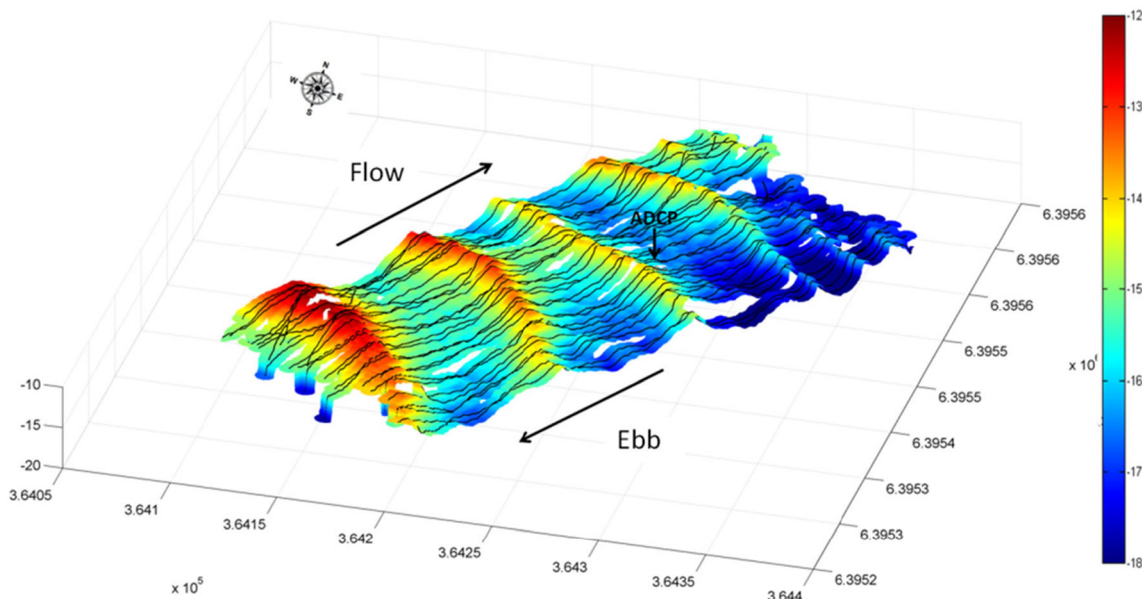

Fig. 3 Bathymetry measured on September 13, 2013. The ADCP position is showed on the selected dune profile
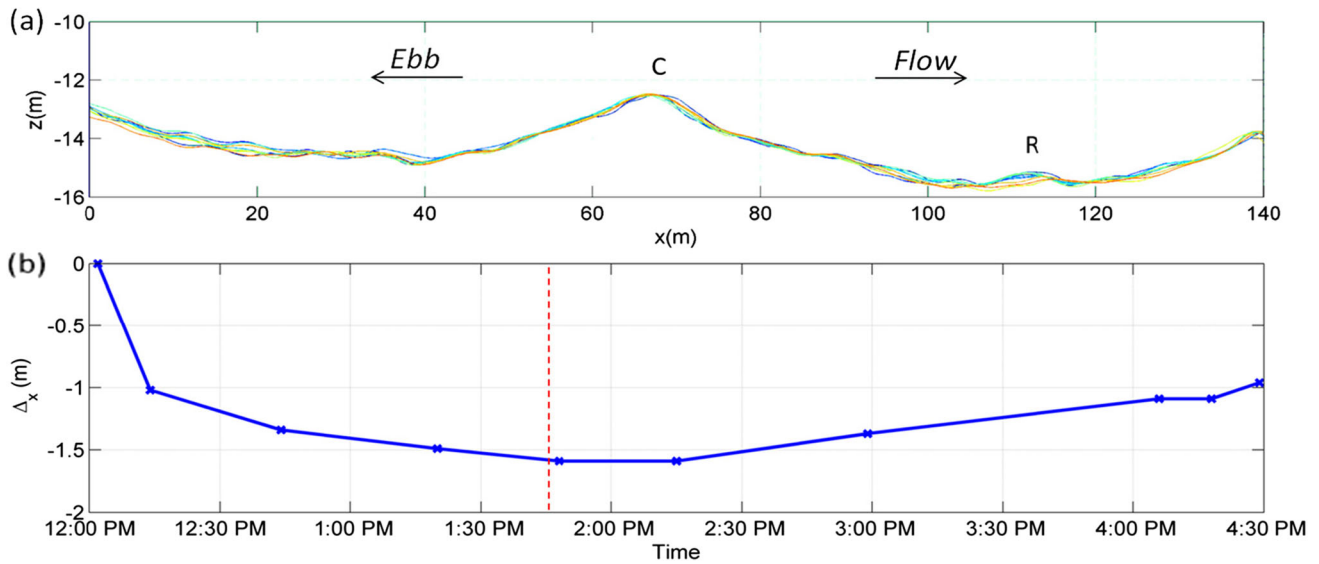
Fig. 4 **a** Dune profile evolution during the mean tide of September 24, 2013. "C" stands for the crest and "R" for a superimposed ripple in the bottom part of the dune profile. The color palette from blue to red describes transects at different times of the tidal phase, from the oldest to the newest. **b** Relative horizontal displacement of the dune crest. The red dotted line corresponds to the date when q_s becomes negligible

cell possibly enhances locally the steepening of the profile on the stoss side. During the period of measurement, the dune crest is moving in the direction of the inlet axis with an average velocity of 0.5 m h^{-1} during ebb tide and 0.4 m h^{-1} during flood tide, leading to horizontal displacements of $\Delta x = -1.55$ m and $\Delta x = 0.6$ m during ebb and flood tides, respectively. Assuming that the mean crest migration rate during the first 2.5 h (1.5 h) and the last 3 h (5 h) of the ebb (flood) tide is constant leads to an accumulated horizontal displacement of $\Delta x = 2.9$ m ($\Delta x = 2.6$ m) during ebb (flood) tide. Δx is most

likely slightly underestimated for the flow tide. Integrating the mean migration rate over the full duration of the ebb and flood tides gives a mean amplitude of the crest horizontal displacement of the order of $|\Delta x| \sim 2.8$ m during the tidal cycle.

The red dotted line in Fig. 4 shows the time when the suspended sediment transport, q_s, has become negligible, around 1:45 pm, due to reduced mean tidal current velocities, $U_0 < 0.7$ m s^{-1}. After that time, the crest stabilizes and starts moving backwards until low tide, around 3 pm. The crest is also moving in the vertical plane (not shown), with
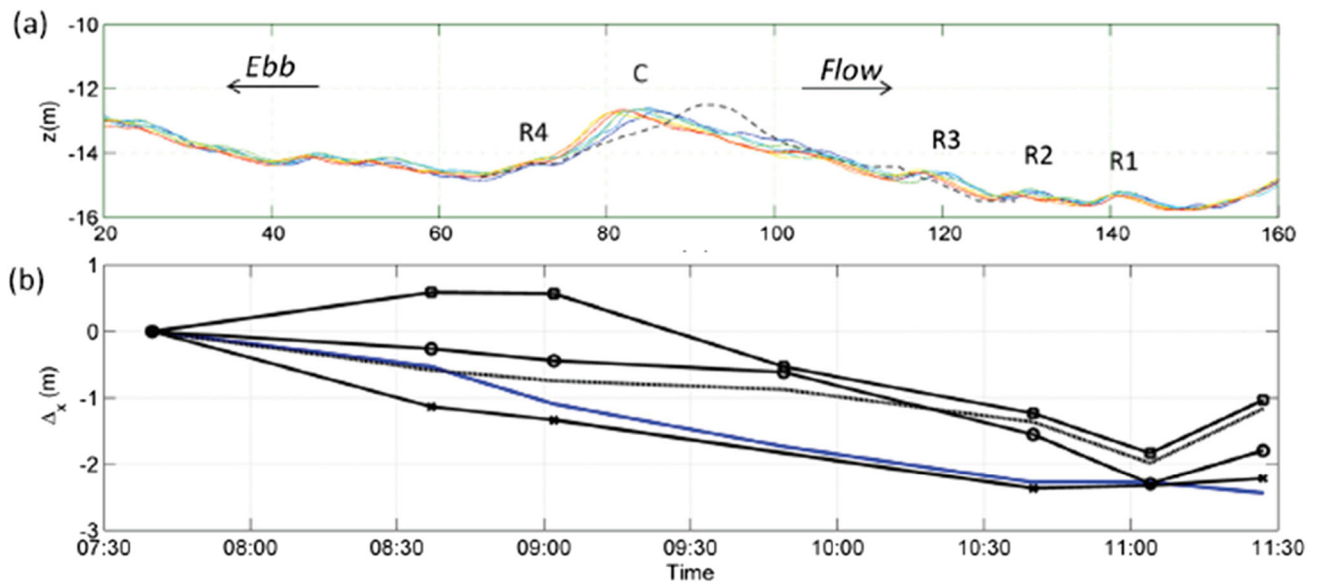

Fig. 5 **a** Dune profile evolution during the spring tide on June 13, 2014. "C" stands for the crest and "R1" to "R4" for the superimposed ripples. The color palette from blue to red describe transects at different times of the tidal phase, from the oldest to the newest. The dotted line represents

the dune profile for the mean tide on September 24, 2013. **b** Relative horizontal displacement of dune and ripple crests. Blue: C; black, –: R1; o-: R2; x-: R3; Ḡ-: R4

Fig. 6 Time series of the mean current velocity, U_0, applied at the western boundary of the domain
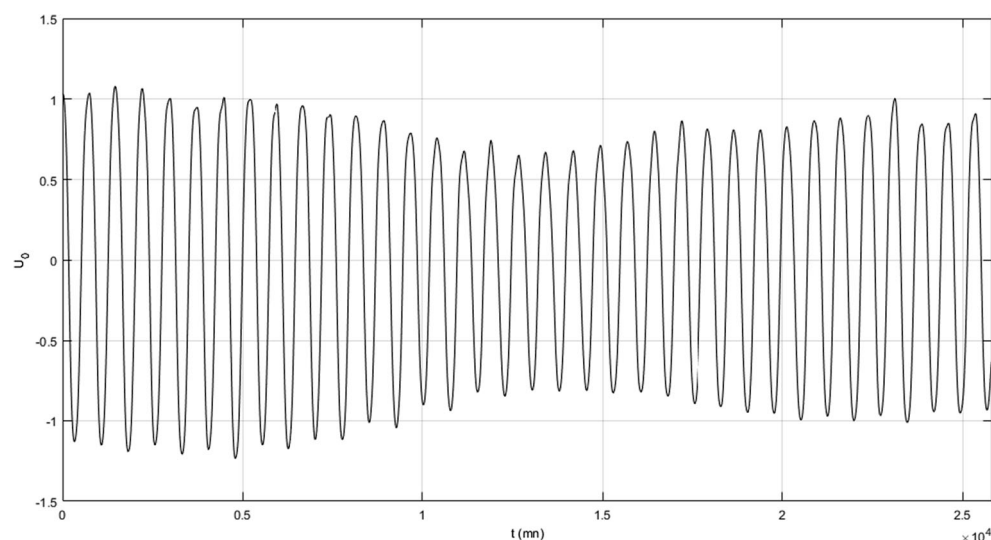
displacements of $\Delta z = -10$ cm before 1:45 pm, and then increases of $\Delta z = 10$ cm after that time. This means that the displacement of the crest, between 1:45 pm and 3 pm, in the opposite direction of the ebb flow, is probably due to the adaptation of the dune profile to milder sediment fluxes conditions, in absence of suspended sediment fluxes that usually flatten the dune profile shape. After 3 pm, the flow is inverting and the crest is slowly moving in the direction of the flow.

Measurements during the spring tide of June 13, 2014, started at 7:30, 1.5 h after high tide. Figure 5 shows the position of the crest, C, and of four superimposed ripples, $R1$ to $R4$. $R1$ to $R3$ are located on the dune stoss side, whether $R4$ is located on the dune front slope. The dune crest is moving horizontally over a distance of $\Delta x = -2.44$ m, at an average rate of 0.65 m h^{-1}. Assuming that the mean migration rate during the measurement period is equal to the mean migration rate for the full ebb tide, leads to a total crest displacement of $\Delta x = -3.8$ m. In the meantime, the vertical position of the dune crest is decreasing by $\Delta z = -0.3$ m (not shown here), due to high suspended sediment fluxes, a consequence of relatively high current velocities, with $U_0 > 0.7$ m s^{-1} until 11:20. The dune profile for mean tide conditions is represented on top of the profile for the spring tide in Fig. 5. During the spring tide, the dune profile asymmetry is strongly marked in the direction of the ebb flow, whether during the mean tide, the profile is less asymmetric. The larger magnitude of the sediment transport in suspension during the spring tide flattens the dune profile. The dune front slope is in the range 12°–15° at the beginning and at the end of the ebb tide, and peaks around mid-ebb tide with values up to 20°. The steep dune front together with the acceleration of the flow above the dune crest potentially enhances the presence of a recirculation cell.

Superimposed ripples have wavelengths between ~ 5 and ~ 15 m and heights between 0.15 and 0.6 m, $R1$ being the smallest and $R3$ being the largest. $R1$ to $R3$ are migrating in the direction of the crest, with migration rates between 0.3 and 0.5 m h^{-1},

respectively, closer to the trough ($R1$) and higher on the dune profile ($R3$). Vertical ripple crest displacements lie between 1 and 5 cm, compared to ripple heights in the range 10–30 cm. $R4$ is migrating in the opposite direction of the ebb current until 9:30, then is changing polarity and start migrating in the direction of the ebb current (Fig. 5). This is the signature of a flow recirculation cell in the lee of the dune front, which was also confirmed by ADCP measurements over the dune front slope around mid-ebb tide. Ripple heights are varying between measurements with amplitudes up to $\Delta z = 4$, 9, and 15 cm for $R1$ to $R3$, respectively. As the tide is changing direction around 11:30, ripples are changing polarity and start moving in the direction of the flow (Fig. 5).

Superimposed ripples were observed in the vicinity of the dune crest with the ALTUS during the June 2014 campaign. The ALTUS was able to detect the migration of ripple crests under the sensor during several tidal cycles, leading to values of ripple migration rates in the range 0.3 to 0.6 m h^{-1}, in line with values retrieved from measurements carried out with the echosounder.

Table 1 Parameters used for the simulation of scenario R. t_i, initial time; N_x, number of grid points in the horizontal direction; L, domain length; H_f, λ_f, mean ripple height and wavelength at the end of the simulation, respectively.

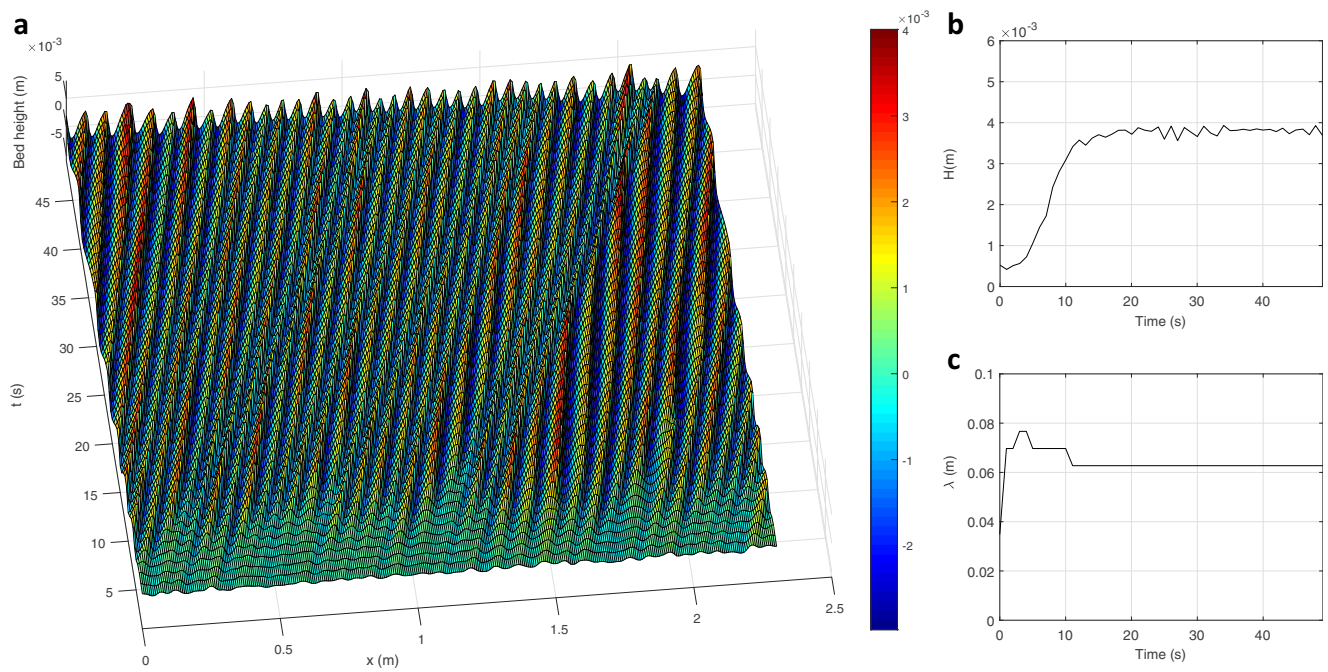| Domain	t_i	N_x	L	H_f	λ_f
1	0	400	2.3	0.015	0.3
2	330	800	12	0.025	0.55
3	430	500	12	0.06	1.1
4	980	400	12	0.26	5.2
5	21,500	800	140	0.6	17

Fig. 7 (**a**) Time evolution of the quasi-flat bed in the early stages for $0\,s < t < 50\,s$. Time series of the evolution of the height (**b**) and of the wavelength (**c**) of the bed perturbations determined by autocorrelation starting with an initially quasi-flat bed

3 Numerical modeling of tidal sand dune dynamics

In this research, we use the model of Doré et al. (2016) with an additional feature in order to take into account tidal forcing conditions. A short description of the model is given in the following.

3.1 Numerical model

The model solves the Reynolds Averaged Navier Stokes equations in the boundary layer, and the turbulence field is calculated with a k-ω scheme (Andersen 1999). The sediment transport module calculates the bedload flux using the formulation of Meyer-Peter and Müller (1948), and the suspended sediment concentration is calculated through an advection-diffusion equation with the bottom concentration calculated from the formulation of Engelund and Fredsøe (1976). The morphological module was developed by Marieu et al. (2008) and is particularly suited to handle flux discontinuities at the crests. The hydrodynamic and morphological modules are decoupled, considering that the adaptation time of the hydrodynamic is small compared to the bed evolution time. The morphological module time step is adjusted during the
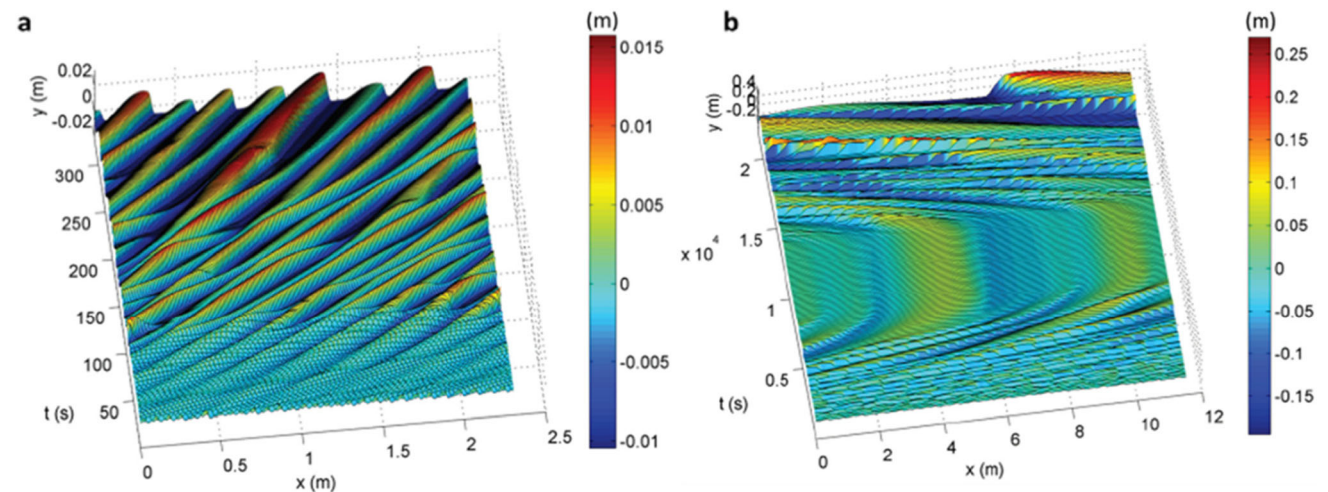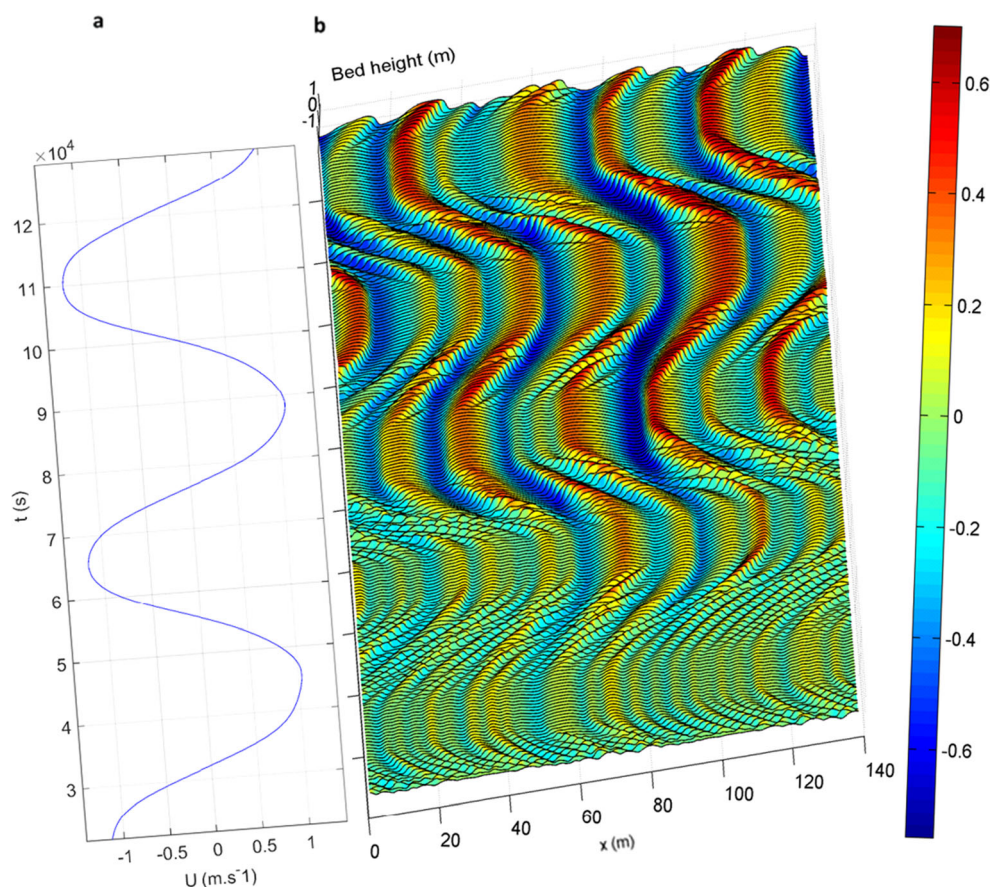

Fig. 8 Time evolution of bed height for $0\,s < t < 330\,s$, domain 1 (**a**) and $330\,s < t < 21,500\,s$, domain 2–4 (**b**)

Fig. 9 Time evolution of the mean current velocity (**a**) and of the bed height (**b**) for $t > 21,500$ s, domain 5

simulation to avoid the occurrence of numerical spurious oscillations. For a detailed description of the model, see Doré et al. (2016).

3.2 Model parameters

To insure realistic simulations, forcing conditions are derived from in situ ADCP and ADV measurements above the dune profile. The free surface is represented by a rigid lid in the model. The discharge is adjusted to retrieve the bottom shear velocity, u^*, assuming a logarithmic profile of the current velocity in the boundary layer, and integrating over the depth. Figure 6 shows time series of the mean current velocity applied in the model at the western boundary. At the bottom boundary, the in situ sand roughness, $k_n = 2$ $d_{50} = 7.75.10^{-4}$ m is used, if not stated otherwise. The simulation starts at mid-flood tide of the first spring tide in the measurements. In the simulations, the flood (ebb) tide is conventionally directed towards the positive (negative) abscissa. The time step in the simulation is $\Delta t = 300$ s.

3.3 Modeled scenarios

Two modeling scenarios were carried out. In the first scenario, R, the bed evolution is simulated starting with a slightly perturbed, quasi-flat bed. The bed evolution encompasses

various orders of magnitudes of bedform wavelengths ($\langle\lambda\rangle$ ~0.08 m to $\langle\lambda\rangle$~17 m), and therefore five numerical models with different domain resolutions are used[1] to avoid prohibitive calculation times (Table 1). The depth is also adjusted for each domain to insure relatively high values of the adimensional depth, kD, so that ripples are not influenced by the free surface. In the second scenario, D, the bottom is covered with dunes of the same size as the dunes observed in situ ($\langle\lambda\rangle$~70 m and $\langle H\rangle$~2 m). The calculation domain has the same characteristics as domain 5 in Table 1. Ripple wavelengths and heights are retrieved using the autocorrelation of the bed profile during the incipient ripple generation phase and using a zero crossing approach at a later stage during the non-linear bed development phase (Doré et al. 2016).

3.4 Results

3.4.1 Scenario R

Incipient ripples Figure 7a shows a focus on the time evolution of the bed height for the first 50 s of the simulation. The model is able to reproduce the incipient ripple generation

---

[1] A resolution of 30–40 grid points per wavelength is recommended (Doré et al. 2016).

Fig. 10 Time evolution of the mean current velocity (**a**) and of the bed slope (**b**) for $t > 21,500\ s$, domain 5
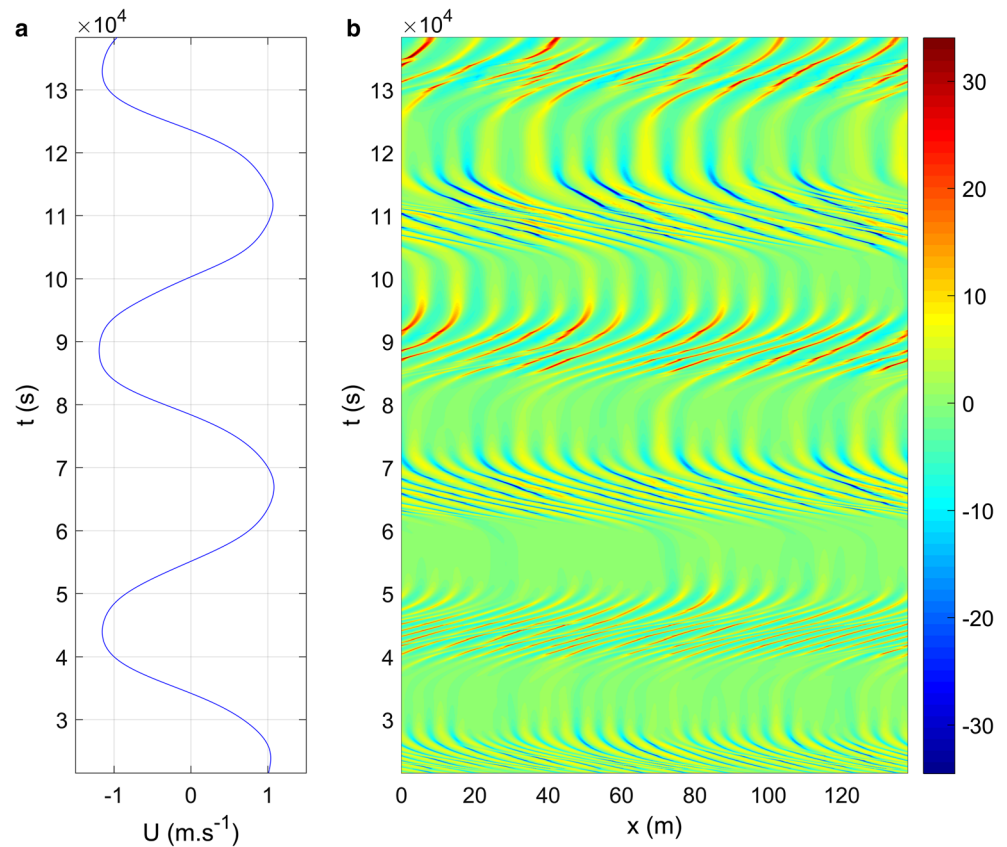
phase, starting with a quasi-flat bed, in the first instants of the simulation. Here, the initial bed is flat with randomly distributed small perturbations ($H = O(d50)$), which is below the dimensions of the incipient ripples observed for similar grain sizes (Coleman and Melville 1996; Raudkivi 1997; Fourrière et al. 2010). Figure 7b, c shows the time evolution of the wavelength, λ, and the height, H, of bedforms retrieved by computing the autocorrelation of the bed profile. This method of analysis enables the relative influence of bedforms of different magnitudes to be correctly evaluated without necessitating any preliminary screening of small bedform data (Coleman and Melville 1994). The position of the secondary maximum of autocorrelation gives the dominant wavelength on the domain, and its amplitude gives the corresponding height. Results show the emergence of ripples with a preferred wavelength, similar to the incipient ripple generation under steady current conditions (Doré et al. 2014; Doré et al. 2016). The evolution in the first stages of the bed evolution is characterized by an exponential growth of the mean geometrical characteristics (Fig. 7b). Incipient ripples reach mean adimensionnal height and wavelength in the interval $13 < H_0/d_{50} < 14$ and $200 < \lambda_0/d_{50} < 260$, H_0 and λ_0 being the incipient ripples mean height and wavelength, in line with previous numerical studies and observations (Doré et al., 2016). Incipient ripple wavelengths depend on the Reynolds particle number, $Re^* = \frac{u^* d}{v}$ (Valance et Langlois

2005; Charru 2006) and therefore will vary depending on the tidal phase when they are generated.

Non-linear bed development Figures 8a, b and 9 respectively show the time evolution of the bed in intervals $0\ s < t < 330\ s$, $330\ s < t < 21,500\ s$, and $13,000\ s < t < 21,500\ s$. Figure 10 shows the time evolution of the bed slope for the interval $13,000\ s < t < 21,500\ s$.

Results of the time evolution of the bed height show a rapid evolution of the incipient ripples in the first stages (Fig. 8a). Merging sequences between ripples quickly occur, like for example in the interval $150\ s < t < 250\ s$. Merging sequences lead to an increase of both ripple heights and lengths, and ripple number is accordingly decreasing in the domain as already described for steady current conditions by Doré et al. (2016). In the first 300 s, the mean statistical wavelength and height reach a value of 0.3 m (4 λ_0) and 0.015 m (4 H_0), respectively.

Migration velocities decrease until $t = 10,000\ s$, due to lower current intensities around high tide (Fig. 8b). Around $t = 13,000\ s$, ripples lose their asymmetry and change polarity, as currents reverse and increase in the direction of the flow (Fig. 8b). Such sequences of inversion of ripples polarity occur at $t = 36,500\ s$, $t = 58,500\ s$, $t = 80,100\ s$, $t = 103,100\ s$, and $t = 125,100\ s$, as shown in Fig. 9, approximately 1.5 h after slack tides, when the mean current intensity exceeds

Fig. 11 Time series of the statistical mean bedform wavelength (**a**) and height (**b**) for the full simulation. The red dotted curves represent equation 1 ($t <$ 20, 000 s) and equation 2 ($t > 20$, 000 s)
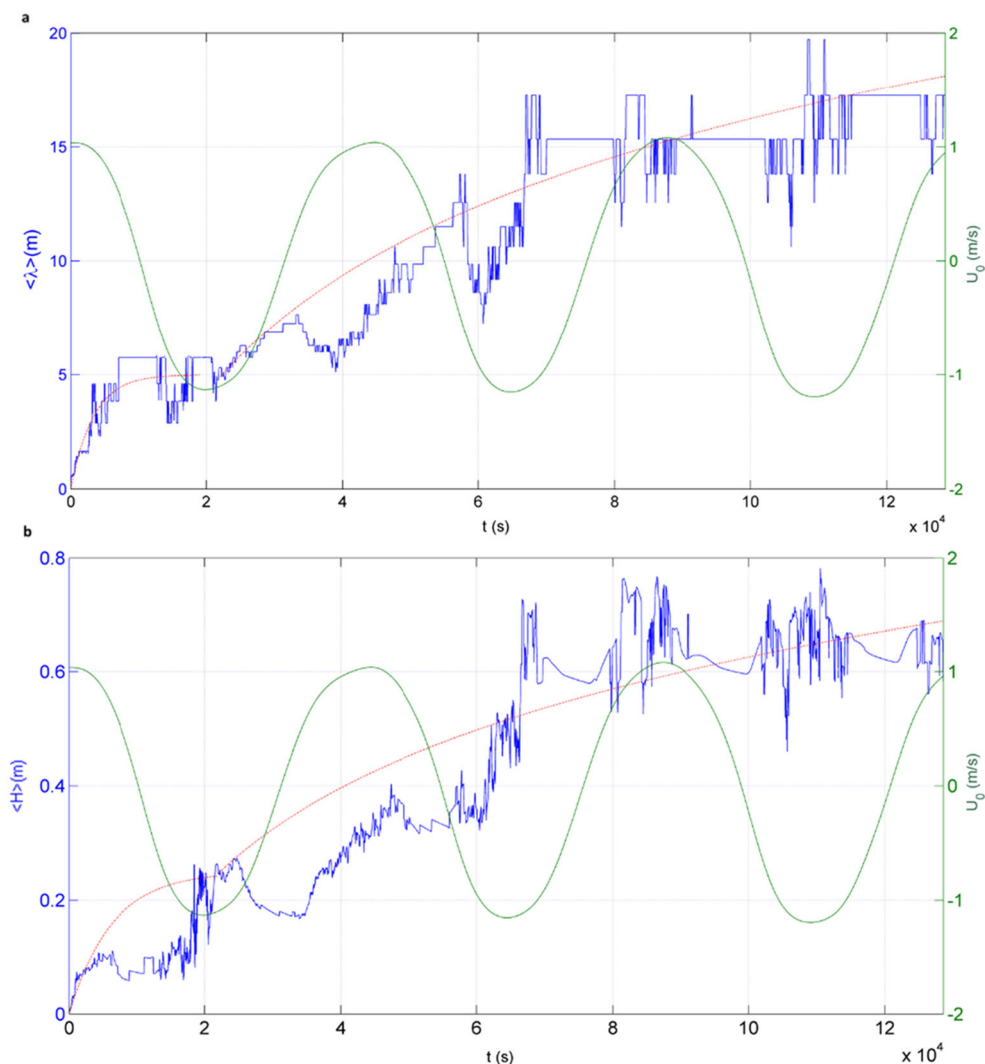
$U_0 = 0.7$ m s^{-1}. Ripples are merging with one another around mid-ebb tides and mid-flood tides, when mean current intensity peaks, with values above $U_0 = 1$ m s^{-1}. Highest bed slope values correspond to the location of ripple crests[2] (Fig. 10). Merging sequences between ripples can be observed each time the number of red and blue lines diminishes in Fig. 10 at around $t = 4, 000s$, $t = 6, 500$ s, and $t = 8, 500$ s. The number of ripples in the domain is 26, 19, 13, 8, and 8 respectively at $t = 3, 000$ s, $t = 5, 500$ s, $t = 7, 500$ s, $t = 9, 500$ s, and $t = 12$, 000 s, decreasing at a slower pace as time goes by (Fig. 10). In the meantime, the adimensional depth drops from $kD = 15$ to $kD = 4.5$. As kD decreases, bedforms are increasingly influenced by the presence of the free surface, which is slowing down their growth (Charru 2013; Doré et al. 2016), and can be considered as being dunes.[3] Merging sequences become scarcer, due to lower migration velocities of larger bedforms.

The time evolution of bedform statistical mean height, $\langle H \rangle$, and wavelength, $\langle \lambda \rangle$, expressed in meters, is shown in Fig. 11. The curve of bedform height evolution clearly shows an alternance of phases of increase around mid-tides and phases of relative stability around slack tides. Periods of increase in mean bedform height correspond to cascading merging sequences that are also clearly visible in Figs. 9 and 10. Wavelengths are also increasing, but with a time lag compared to heights, as they slowly adapt to the higher heights of the merged bedforms (40, 000 < t < 60, 000 s, Fig. 11), in line with Doré et al. (2016).

Beyond the brief incipient ripple generation phase, which is characterized by an exponential growth (Doré et al. 2016), both curves of $\langle H \rangle$ and $\langle \lambda \rangle$ show two distinct phases of evolution. During the first 5.5 h ($t <$ 20, 000 s), the time evolution of both statistical wave height and wavelength can be approximated by the unified relation for bedform development of Perillo et al. (2014), as follows[4]:

---

[2] The bed slope at the crest corresponds to the angle of repose of the sediment.
[3] In the following, the more generic term "bedform" is used, as bedforms can be either ripples or dunes depending on the stage of evolution.

[4] Trend lines are chosen in order to fit the values of mean wavelengths and heights around mid-tide.

Fig. 12 (**a**) Time evolution of the bed height. (**b**) Time series of the mean dune height (black) and of the mean tidal current velocity (blue) for $0\,s < t < 190{,}000\,s$
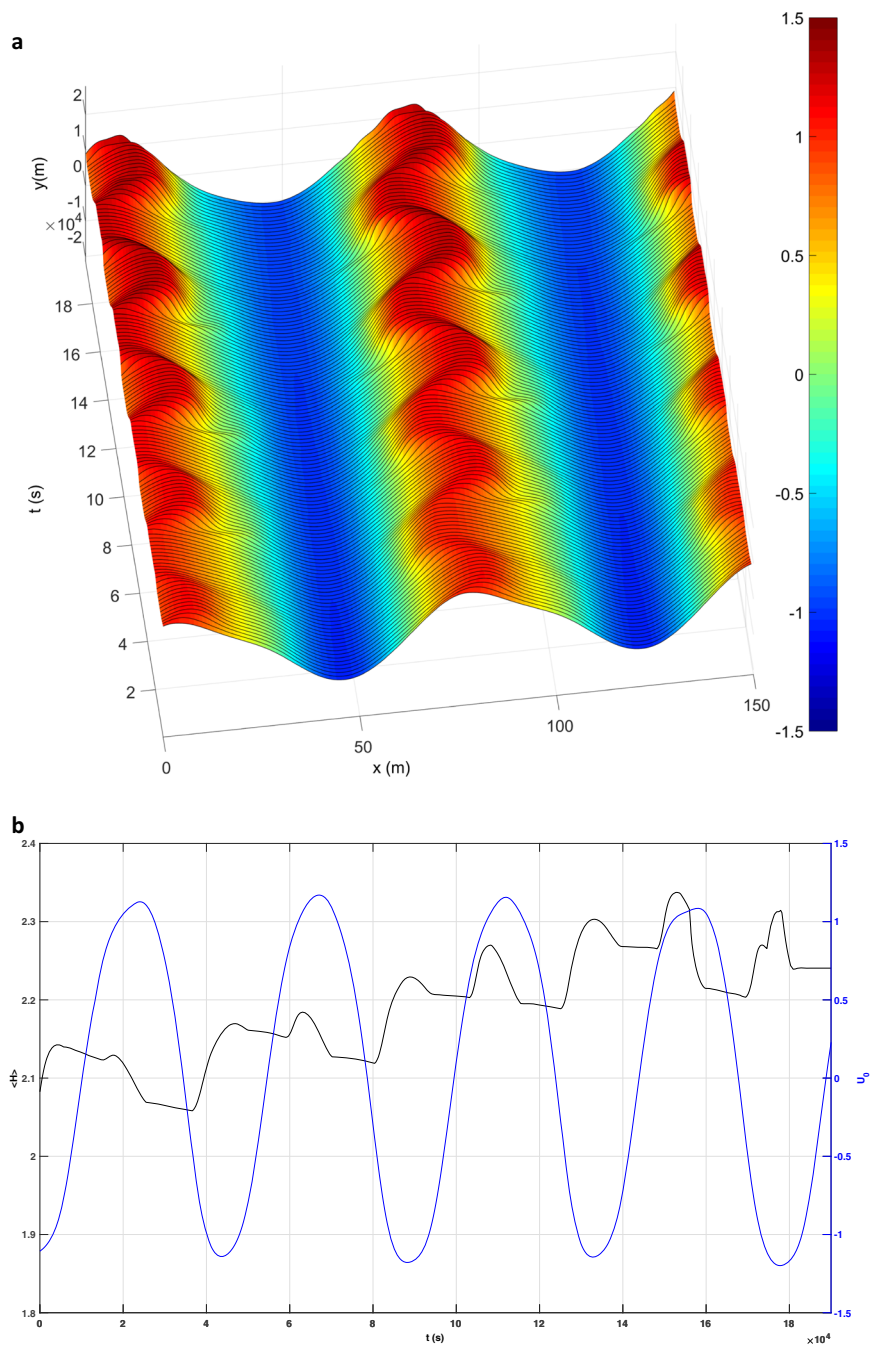
$$\langle \lambda, H \rangle = \langle \lambda_{t5.5}, H_{t5.5} \rangle \left(1 - e^{-C_{\lambda,h}t}\right) \quad (1)$$

t being the time in seconds, $\langle \lambda_{t5.5}, H_{t5.5} \rangle$ being the bedform statistical mean wavelength and height, in meters, at $t = 5.5\,h$ $(20{,}000\,s)$. C_λ and C_h are calibrating coefficients for wavelength and height evolution, respectively.[5] For $t > 20{,}000\,s$, a relation similar to Eq. 1 would overestimate the bed evolution, which is better approximated by the following logarithmic relation:

$$\langle \lambda, H \rangle = \langle \lambda_e, H_e \rangle (a\ln(t) - 1) \quad (2)$$

$<\lambda_e>$ and $<H_e>$ being the statistical mean wavelength and height at equilibrium, respectively, with $<\lambda_e> = 70\,m$ and $<H_e> = 2.2\,m$, in agreement with in situ values, and $a = \frac{2}{\ln T_e} = 0.11$, T_e being the time to equilibrium, in seconds. Equation 1 corresponds to a situation when frequent merging sequences occur whether Eq. 2 accurately represents the bottom evolution when merging sequences are more scarce and bedform growth is mostly linked to sediment fluxes intensity. Equation 2 gives an equilibrium time of $T_e = 2.5$ years.

---

[5] $C_\lambda = 0.0003$ and $C_h = 0.0001$

T_e is in good agreement with the time that would be needed to generate a dune of volume $V_e = \lambda_e \cdot H_e/2$ ($\langle\lambda_e, H_e\rangle = \langle 70, 2\rangle$), the tidal averaged net sediment fluxes measured at the dune crest, $q = 1.10^{-6} m^3 s^{-1}$.

Bedform mean statistical height and wavelength reach the values of $\langle H\rangle = 0.6$ m (0.3 m) and $\langle\lambda\rangle = 17$ m (8 m) after a time interval of 35 h (15 h). These values are close to wavelengths and heights of superimposed ripples observed in situ on the dune stoss side and in the dune trough (Fig. 5). Modeled bedform heights show variations in amplitude up to $\Delta z =$ 15 cm between mid-tides and slack-tides (Fig. 8), which are of the same order of magnitude as variations measured in situ (Section 2.4). In the simulation, bedforms are migrating in the direction of the ebb flow, which is also the direction of the net sediment transport measured in situ.

3.4.2 Scenario D

In scenario D, we use the numerical model to simulate the dynamics of larger dunes forced by a tidal current. The forcing conditions are the same as in scenario R. A parametric study to test the effects of the bed roughness on the flow and the induced bed evolution was first carried out. The results show that for lower bed roughness values in the range $k_n = 1 - 2.5\, d_{50}$, dune crests have large horizontal movements leading to changes of polarity of dune profiles, which is not observed in situ. Modeled dune heights are also increasing to much larger values than those in the observations. For $k_n > 20\, d_{50}$, the modeled dune field is quickly eroded and modeled dune heights are much lower than observed dune heights. A bed roughness of $k_n = 10\, d_{50}$ was finally used in the simulation to model the drag effects due to roughness elements that are present on the dune profile. Sediment fluxes are modeled by taking into account the sand surface roughness. Sediment fluxes are calibrated by comparing with sediment fluxes measured at the dune crest in situ.

Figure 12a shows the time evolution of the dune field over several tidal cycles, and Fig. 12b shows the time evolution of dune statistical mean height together with the mean tidal current velocity. Figure 13 shows the time evolution of the bed slope. Ebb (flow) currents are directed to the left (right).

Fig. 13 Time evolution of the of the bed slope for $0\ s < t < 190,000\ s$
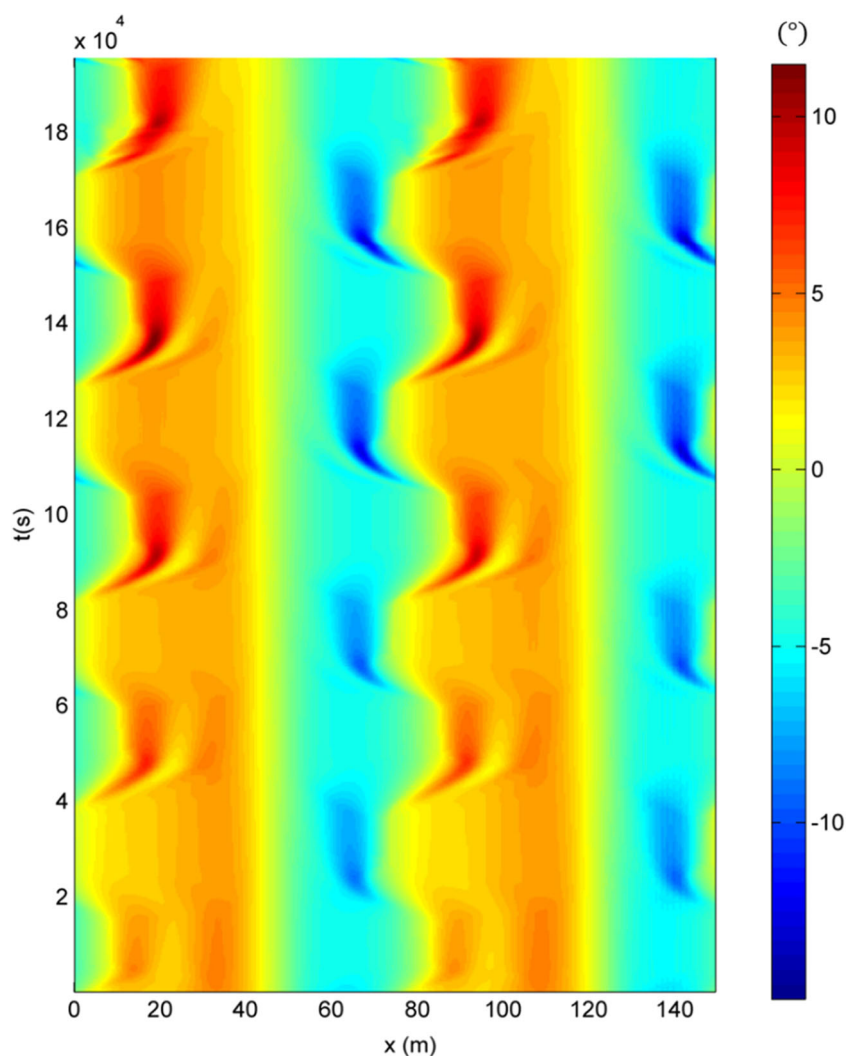
Dune net migration rates have values of a few centimeters per day. Even though results seem to show that the dune field is slowly migrating in the direction of the ebb flow, this should still be confirmed through longer simulation times. Dune crests are oscillating according to ebb and flood tides but keep their asymmetry in the direction of the ebb flow. Crest horizontal displacements of a few meters are of the same order of magnitude as in the observations (Section 2.4). During the first hours of flow phases, the dune profile is bended on the stoss side (around $x = 100\ m$, Figs. 12a and 13), reproducing the "cat back" dune profile shape in agreement with observations (Section 2.4). Dune heights are generally larger during flood tides (Fig. 12b). During ebb tides, lower water depths and higher bottom shear stresses enhance suspended sediment transport which flattens dune profiles (Tjerry and Fredsøe 2005). The modeled vertical displacements of dune crests of a few tens of centimeters during a tidal cycle (Fig. 12b) are of the same order of magnitude as the ones measured in situ (Section 2.4). Variation of dune lee angles, on dune fronts, varies from $\alpha \approx 15°$ at mid-tides down to $\alpha \approx 5°$ at slack tides, with α the dune lee angle, in good agreement with observations (Section 2.4).

4 Conclusions

Tidal dune dynamics was observed through a series of measurements in the inlet of Arcachon, southwest France. Observations showed that the inlet bottom is covered by a field of tidal sand dunes with an average wavelength of five to eight times the mean water depth. Superimposed ripples are observed on the dune stoss and lee sides and have wavelengths of an order of magnitude smaller than dunes. Measurements of bathymetry transects along the dune profile for two tidal cycles showed that dune crests are oscillating horizontally with an amplitude of a few meters, and are moving vertically with an amplitude of a few tens of centimeters. Dune profile asymmetry is more pronounced during spring tides, and crest displacements are larger than those for average tides. Superimposed ripples are migrating on the dune profile with velocities of a few tens of centimeters per hour and change polarity between ebb tide and flood tide.

A 2D RANS model was used to simulate the evolution of an erodible non-cohesive sand bed forced by tidal currents. The initial phase of incipient ripples generation was successfully reproduced, and results are in line with both analytical models and experimentations. We showed that small perturbations are exponentially growing in height; then, after a rapid period of tens of seconds, the initial ripple field has emerged. Beyond the initial linear phase, the simulation of the non-linear bed evolution compared well with observations in situ. The results showed that the bed growth is insured by cascading bedform merging sequences occurring mainly at mid-tides, when tidal currents have the highest values. Simulated bedform wavelengths and heights are of the same order of magnitude as for superimposed ripples observed in situ. Two evolution equations of the bed were derived corresponding respectively to a situation when bed growth is insured by frequent merging sequences and when bed growth is mostly linked to sediment fluxes intensity. The time to equilibrium for larger dunes was estimated, based on an equation of the bed evolution that was derived. In the simulation, bedforms migrated in the direction of the net sediment transport, which was also observed in situ.

The model was used to simulate a field of large dunes, with similar geometrical characteristics as dunes found in situ, under tidal forcing conditions. Dunes kept their asymmetry during the simulation, crests were moving back and forth depending on the tidal phase, and dunes seemed to slowly migrate in the direction of the ebb tide. In the simulation, ebb-oriented dune profiles exhibited a "cat back shape" during flood tide, which was also observed in situ. These results show the ability of the model to reproduce tidal sand dune dynamics and open promising perspectives in terms of numerical modeling of tidal sand dune morphodynamic evolution.

References

Andersen KH (1999). The dynamics of ripples beneath surface waves and topics in shell models of turbulence, Ph.D. dissertation, Det Naturvidenskabelige Fakultet Københavns Universitet

Barrie JV, Hill PR, Conway KW, Iwanowska K, Picard K (2005) Georgia basin: seabed features and marine geohazards. Geosci Can 32:145–156

Baas JH (1994) A flume study on the development and equilibrium morphology of current ripples in very fine sand. Sedimentology 41:185–209

Baas JH (1999) An empirical model for the development and equilibrium morphology of current ripples in fine sand. Sedimentology 46:123–138

Barnard PL, Hanes DM, Rubin DM, Kvitek RG (2006) Giant sand waves at the mouth of San Francisco Bay. Eos, Transactions American Geophysical Union 87(29):285

Barnard PL, Erikson LH, Rubin DM, Dartnell P, Kvitek RG (2012) Analyzing bedforms mapped using multibeam sonar to determine regional bedload sediment transport patterns in the San Francisco bay coastal system. Mar Geol 345:72–95. https://doi.org/10.1016/j.margeo.2012.10.011

Barrie JV, Conway KW (2014) Seabed characterization for the development of marine renewable energy on the Pacific margin of Canada. Continental Shelf Research 83:45–52

Butel R, Dupuis H, Bonneton P (2002) Spatial variability of wave conditions on the French Atlantic coast using in situ data. J Coast Res Spec Issue 36:93–108

Belderson RH, Johnson MA, Kenyon NH (1982) Bedforms. Chapman and Hall, London, pp 27–57

Best J (2005) The fluid dynamics of river dunes: a review and some future research directions. J Geophys Res 110:F04S02. https://doi.org/10.1029/2004JF000218

Charru F (2006) Selection of the ripple length on a granular bed sheared by a liquid flow. Physics of Fluids 18 (12):121508

Charru F (2013) Sand ripples and dunes. Annu Rev Fluid Mech 45:469–493. https://doi.org/10.1146/annurev-fluid-011212-140806

Coleman SE, Melville BW (1994) Bed-form development. J Hydraul Eng 120:544–560

Coleman SE, Melville BW (1996) initiation of bed forms on a flat sand bed. J Hydraul Eng 122:301–310

Doré A, Bonneton P, Marieu V, Garlan T (2014) Modélisation de l'évolution morphodynamique des dunes sous-marines. Proceedings des XIII èmes JNGCGC, Dunkerque 2–4 Juillet 2014, 289–296 https://doi.org/10.5150/jngcgc2014.032.

Doré A (2015) Modélisation de l'évolution morhodynamique des dunes sous-marines, Ph.D. dissertation, Ecole Doctorale Sciences de l'Environnement de l'université de Bordeaux

Doré A, Bonneton P, Marieu V, Garlan T (2016) Numerical modeling of subaqueous sand dunes morphodynamics. J Geophys Res Earth Surf 121:565–587. https://doi.org/10.1002/2015JF003689

Dreano J, Valance A, Lague D, Cassar C (2010) Experimental study on transient and steady-state dynamics of bedforms in supply limited configuration. Earth Surf Process Landf 35:1730–1743. https://doi.org/10.1002/esp.2085

Engelund F (1966) Hydraulic resistance of alluvial streams. J Hydraul Div HY4:287–297

Engelund F, Fredsøe J (1976) A sediment transport model for straight alluvial channels. Nord Hydrol 7:293–306

Ernstsen VB, Noormets R, Winter C, Hebbeln D, Bartholoma A, Flemming BW, Bartholdy J (2006) Quantification of dune dynamics during a tidal cycle in an inlet channel of the Danish Wadden Sea. Geo-Mar Lett 26:151–163. https://doi.org/10.1007/s00367-006-0025-3

Fourrière A, Claudin P, Andreotti B (2010) Bedforms in a turbulent stream: formation of ripples by primary linear instability and of dunes by nonlinear pattern coarsening. J Fluid Mech 649:287–328. https://doi.org/10.1017/S0022112009993466

Fredsøe J (1982) Shape and dimensions of stationary dunes in rivers. J Hydraul Div 8:932–947. https://doi.org/10.1017/S0022112074001960

Fredsøe J, Deigaard R (1992) Mechanics of coastal sediment transport. World Scientific, Singapore

Knaapen MAF, Van Bergen Henegouw CN, Hu YY (2002) Quantifying bedform migration using multi-beam sonar. Geo-Mar Lett 46

Kostaschuk R, Best J (2005) Response of sand dunes to variations in tidal flow: Fraser estuary, Canada. J Geophys Res 110:F04S04. https://doi.org/10.1029/2004JF000176

Langhorne DN (1982) A study of the dynamics of a marine sandwave. Sedimentology 29:571–594

Langlois V, Valance A (2007) Initiation and evolution of current ripples on a flat sand bed under turbulent water flow. Eur Phys J E 22:201–208

Lefebvre A, Ernstsen VB, Winter C (2013) Estimation of roughness length sand flow separation over compound bedforms in a natural

tidal inlet. Cont Shelf Res 61-62:98–111. https://doi.org/10.1016/j.csr.2013.04.030

Li MZ, Shaw JS, Todd BJ, Kostylev VE, Wu Y (2014) Sediment transport and development of banner banks and sandwaves in an extreme tidal system: upper bay of Fundy, Canada. Cont Shelf Res 83:86–107. https://doi.org/10.1016/j.csr.2013.08.007

Marieu V, Bonneton P, Foster DL, Arduhin F (2008) Modeling of vortex ripple morphodynamics. J Geophys Res 113:C09007

Meyer-Peter E, Müller R (1948) Formulas for bed-load transport, Proceeding of the International Association of Hydraulic Research. 3rd Annual Conference, Stockholm, pp 39–64

Morelissen R, Hulscher SJMH, Knaapen MAF, Nemeth AA, Bijker R (2003) Mathematical modelling of sand wave migration and the interaction with pipelines. Coast Eng 48:197–209. https://doi.org/10.1016/S0378-3839(03)00028-0

Nabi M, Vriend HJD, Mosselman E, Sloff CJ, Shimizu Y (2013) Detailed simulation of morphodynamics: 3. ripples and dunes. Water Resour Res 49:1–14. https://doi.org/10.1002/wrcr.20457

Niemann SL, Fredsoe J, Jacobsen NG (2011) Sand dunes in steady flow at low Froude numbers: dune height evolution and flow resistance. J Hydraul Eng 137:5–14

Paarlberg AJ, Dohmen-Janssen CM, Hulscher SJMH, Termes P (2009) Modeling river dune evolution using a parameterization of flow separation. Journal of Geophysical Research 114(F1). https://doi.org/10.1029/2007JF000910

Pedreros R, Lecacheux S, Sottolichio A, Romieu E, Idier D, Salles P, Delattre M (2008) Caractérisation des vagues dans les passes du bassin d'Arcachon, Proceedings des Xèmes JNGCGC, Sophia Antipolis 14–16 Octobre 2008, 273–282. https://doi.org/10.5150/jngcgc.2008.026-P

Perillo MM, Best JL, Yokokawa M, Sekiguchi T, Takagawa T, Garcia MH (2014) A unified model for bedform development and equilibrium under unidirectional, oscillatory and combined-flows. Sedimentology 61:2063–2085. https://doi.org/10.1111/sed.12129

Raudkivi AJ (1997) Ripples on stream bed. J Hydraul Eng 123:58–64

Rubin DM, McCulloch DS (1980) Single and superimposed bedforms: a synthesis of San Francisco bay and flume observations. Sediment Geol 26:207–231

Thauront F (1995) Les transits sédimentaires subtidaux dans les passes internes du bassin d'Arcachon, Ph.D. dissertation, Université de Bordeaux 1

Tjerry S, Fredsøe J (2005) Calculation of dune morphology. J Geophys Res 110:FO4013

Todd BJ, Shaw J, Li MZ, Kostylev VE, Wu Y (2014) Distribution of subtidal sedimentary bedforms in a macrotidal setting: The Bay of Fundy, Atlantic Canada. Cont Shelf Res 83:64–85

Valance A, Langlois V (2005) Ripple formation over a sand bed submitted to a laminar shear flow. The European Physical Journal B 43(2):283–294

Vantorre M, Lataire E, Candries M, van Doorn J, van Heel D (2013) An equivalent bottom for navigation above irregular bottoms, Van Lancker, V. and Garlan, T. (Eds), 2013. MARID 2013. Fourth International Conference on Marine and River Dune Dynamics, 301–308

Whitehouse RJS, Damgaard JS, Langhorne N (2000) Sandwaves and seabed engineering: the application to submarine cables, Proceeding of Marine Sandwave Dynamics 2000, MARID, 227–234.